



Pore-scale lattice Boltzmann simulation of CO₂-CH₄ displacement in shale matrix

Jian Wu^a, Yixiang Gan^{a,b}, Zhang Shi^c, Pengyu Huang^{a,d}, Luming Shen^{a,*}

^a School of Civil Engineering, The University of Sydney, NSW, 2006, Australia

^b Sydney Nano Institute, The University of Sydney, NSW, 2006, Australia

^c School of Mechanical and Mining Engineering, The University of Queensland, St Lucia, QLD, 4072, Australia

^d Hard Rock Mining, CSIRO Mineral Resources, QCAT, 1 Technology Court, Pullenvale, QLD, 4069, Australia

ARTICLE INFO

Handling Editor: Wojciech Stanek

Keywords:

Shale gas recovery
CO₂-CH₄ displacement
Gas adsorption
LBM
Nanoporous media

ABSTRACT

This study couples the Navier-Stokes and multicomponent advection-diffusion equations within the lattice Boltzmann method (LBM) to innovatively simulate the CO₂-CH₄ displacement in nanoporous shale matrix. In the LBM simulations of CO₂ injection into heterogenous CH₄-saturated nanoporous media, gas movements are modeled by two separate advection-diffusion lattices driven by the velocity solved from the third Navier-Stokes lattice. Langmuir adsorption kinetics is employed at the fluid-solid interfaces to simulate the mass exchange between the bulk free space and the solid matrix. Mass transfer inside the solid matrix is considered with adsorption and diffusion parameters obtained from molecular dynamics studies. CO₂ adsorption and CH₄ desorption are simulated simultaneously. The coupling scheme is successfully validated for advection, diffusion, and surface adsorption. Results show that the global mass transfer process is sensitive to intra-matrix diffusion. When the solid diffusion rate is $\sim 10^{-4}$ of the bulk one, selectivity can significantly impact the outflux concentration. Changing the CO₂ adsorption rate constant 0.1–10 times nearly has no impact on gas adsorption in the solids. In comparison, the CH₄ desorption rate constant strongly correlates to the CH₄ desorption pathway. Increasing the particle size under a given porosity may benefit advection and lead to fast adsorption/desorption in the solids.

1. Introduction

Shale gas contributes to a significant portion of the global energy supply with a growing interest in more countries. One of the biggest challenges associated with shale gas exploitation is the production of adsorbed gas from nanopores within the organic matrix, which consists of 20–80% of total gas held in the shale [1,2]. Apart from horizontal drilling and hydraulic fracturing, CO₂ injection has shown great potential in enhancing the recovery of adsorbed CH₄ [3–6], leading up to 26% more CH₄ production after primary recovery and over 60% of injected CO₂ being sequestered after flooding [7]. CO₂-enhanced shale gas recovery (EGR) is a dynamic displacement process governed by the pressure gradient and the competitive adsorption between CO₂ and CH₄ [2,7–9]. Therefore, it is important to understand the fundamental mechanisms of CO₂-CH₄ transport, displacement, and adsorption/desorption in nanoporous media consisting of complex geometries.

Gas flow and transport have been widely studied by molecular

dynamics (MD) in a single slit pore, which focuses on molecular-level interactions of gas-gas, solid-solid, and gas-solid [10,11]. MD has the advantage of capturing nanopore-scale gas characteristics (e.g., adsorption, diffusion, and surface slip) naturally by only defining the atomic force fields. Pore pressure and slit size are the two most important factors controlling nanoscale gas transport. Yu et al. [12] simulated methane flow in 2 nm, 6 nm, and 10 nm calcite slit pores and found that pore pressure and slit size determined the individual flux contribution from viscous flow, Knudsen diffusion, and surface diffusion. Nan et al. [13] observed that the gas slip length decreased hyperbolically with increasing pore pressure and size in 2–20 nm graphene slit pores. Gas-solid interaction energies at the pore walls impact gas slip flow as well. It is reported that gas slippage may be absent in the inorganic (e.g., quartz, calcite, and montmorillonite) nanopores due to the large fluctuation of the gas-solid interaction energy [14–16]. Similarly, surface roughness causes heterogeneous gas-solid interaction forces and can diminish gas slippage at the pore walls [17–21]. Moreover, MD is

* Corresponding author.

E-mail address: luming.shen@sydney.edu.au (L. Shen).

<https://doi.org/10.1016/j.energy.2023.127991>

Received 4 April 2023; Received in revised form 19 May 2023; Accepted 30 May 2023

Available online 30 May 2023

0360-5442/© 2023 The Authors. Published by Elsevier Ltd. This is an open access article under the CC BY license (<http://creativecommons.org/licenses/by/4.0/>).

extended to investigate multiphase and multicomponent flow, such as the gas-liquid displacement in CO₂/N₂ flooding for enhanced oil recovery [22], miscible CO₂-octane flow [23], and hydrocarbon mixture transport [24], etc. Despite the fact that MD has been a very successful tool in revealing the fundamental mechanisms of gas transport in nanopores, it is limited by the simulation size and duration due to its high computational cost. It cannot be used to study gas flow and transport in complex pore structures at the microscale.

The lattice Boltzmann method (LBM), as a mesoscopic method bridging the nano- and macro-scales, is fundamentally based on the evolution of the discrete-velocity distribution function (i.e., particle population) [25,26]. It is well suited to deal with irregular geometries like porous media and can achieve multi-physics coupling to simulate multiphase and multicomponent flow [25,27,28]. For instance, Zhou et al. [29] upscaled the results from MD simulations into the LBM through a local adsorption density parameter to investigate the effects of adsorption layer and surface diffusion on gas flow and transport in nanoporous shale matrix. There are various strategies to simulate shale gas flow in the LBM, which usually involve the development of slip flow boundary conditions, Knudsen layer, and surface adsorption/desorption [26]. The major types of boundary conditions for gas slippage are bounce-back (BB), Maxwellian diffuse reflection (MDR), and Langmuir slip (LS) [26,30]. They are often implemented in a combined form to control the boundary slip with more accuracy [29,31,32]. The Knudsen layer effect is generally mimicked by deriving local relaxation time from the Knudsen number considering the gas distance from the solid walls [30,33]. Surface adsorption in shale can be simulated by adding an extra gas-solid interaction force into the particle evolution function [34,35].

The Navier-Stokes (NSE) and advection-diffusion equations (ADE) are often coupled in the LBM to investigate single-component gas migration and gas-solid adsorption in 2D porous media [36–42]. Zakirov and Khranchenkov [38] investigated the effect of pore-scale heterogeneity on the dynamic gas adsorption coupled with Peclet number, porosity, adsorption rate constant, and absolute permeability, respectively. Peng et al. [39] studied the desorption-diffusion of methane from coal matrix and gas migration within fractures/micro-pores. Their results indicated that the increased specific surface area and average pore size by hydraulic fracturing could lead to more efficient gas production. Zhou et al. [40] developed three typical kinetic concentration boundary conditions (i.e., Dirichlet, constant concentration-flux, and mixed condition) to simulate the adsorption process at gas-solid interfaces. With the Langmuir adsorption kinetics, they found that the solid adsorption was nearly independent of porosity but changed with pore size in a simplified 2D porous structure composed of squares. They further investigated the gas-solid adsorption process in random porous media with varying porosities and particle sizes reconstructed by the Quartet Structure Generation Set (QSGS) method [41] and argued that external and internal mass transfer resistances were crucial factors controlling the overall adsorption process. Zhang and Sun [42] modified the NSE-ADE LBM coupling scheme by subtracting the adsorbed gas amount from the NSE lattice distribution function to consider the impact of dynamic adsorption on flow velocity. In addition, they proposed to link this LBM coupling scheme with pore network modeling so that the disordered rock pore structures could be preserved in flow simulation.

The NSE-ADE coupling scheme in the LBM is also adopted for multiphase and multicomponent flow only in a few cases [43–45]. For example, Jiang and Xu [43] employed the Shan-Chen model to solve the immiscible CO₂-water flow field and coupled it with mass and heat transfer equations. Wang et al. [44] extended the coupled single-component NSE-ADE LB model to study the separation and selectivity of CO₂-CH₄ gas mixtures in copper (II)-benzene-1,3,5-tricarboxylate (CU-BTC) membranes. They used the grand canonical Monte Carlo (GCMC) method to obtain the Langmuir adsorption parameters for CO₂ and CH₄, which could then be incorporated into the LB model to calculate the selectivity subject to porous media structure. Xia [45] built a coupled model of fluid flow, heat transfer, and mass

transport to investigate the viscous fingering during miscible displacement in porous media generated from micro-CT images.

To our knowledge, the coupled NSE-ADE scheme is still limited to single-component gas transport and has not yet been implemented into the LBM to investigate the dynamic CO₂-CH₄ displacement process in complex porous media. Single-component gas transport is suitable for the investigation of microscale shale gas flow. However, in the case of CO₂-EGR, CO₂ adsorption and CH₄ desorption usually take place simultaneously. It is needed to understand the relation between CH₄ production and CO₂ storage. In this study, we have implemented the NSE-ADE coupling scheme into the LBM to realize CO₂ injection into heterogeneous CH₄-saturated porous media. An NSE lattice is coupled to two ADE lattices (one for each gas component) through the advective flow velocity, and the two ADE lattices are coupled in a simple way to achieve the competitive adsorption/desorption of CO₂ and CH₄. The LB model is first validated against three representative mass transfer problems with analytical solutions and compared with an experiment of CO₂-CH₄ mixture flow through a reaction bed. It is then adopted to simulate the CO₂-CH₄ displacement in porous media of varied pore structures. The CO₂ adsorption and CH₄ desorption pathways in bulk free space and solids are examined in response to several selected parameters.

2. Computational methods

2.1. Navier-Stokes flow

The CO₂-CH₄ gas mixture is driven by an external flow field, which is simulated as a fictitious carrier fluid that conserves mass and momentum. The fluid flow of the CO₂-CH₄ mixture is described by the Navier-Stokes equations as

$$\partial_t \rho + \nabla \cdot (\rho \mathbf{u}) = 0 \quad (1)$$

$$\partial_t (\rho \mathbf{u}) + \nabla \cdot (\rho \mathbf{u} \mathbf{u}) = -\nabla p + \nabla \cdot \boldsymbol{\sigma} \quad (2)$$

where \mathbf{u} , p , ρ are fluid velocity, pressure and density, respectively, and $\boldsymbol{\sigma}$ is the viscous stress tensor. The physical space is discretized into a set of lattice nodes in the LBM solutions and the D2Q9 (two-dimensional and nine-velocity) lattice model is adopted to solve the discrete lattice velocity sets in the nine directions shown by the following vectors

$$\begin{cases} \text{Central : } \mathbf{e}_0 = (0, 0) \\ \text{Othogonal : } \mathbf{e}_1 = (1, 0); \mathbf{e}_2 = (0, 1); \mathbf{e}_3 = (-1, 0); \mathbf{e}_4 = (0, -1) \\ \text{Diagonal : } \mathbf{e}_5 = (1, 1); \mathbf{e}_6 = (-1, 1); \mathbf{e}_7 = (-1, -1); \mathbf{e}_8 = (1, -1) \end{cases}$$

Utilizing the single-relaxation time Bhatnagar-Gross-Krook (BGK) collision operator [46], the evolution of the particle distribution function f_i with time t is calculated as

$$f_i(\mathbf{r} + \Delta t \mathbf{e}_i, t + \Delta t) - f_i(\mathbf{r}, t) = -\frac{1}{\tau_f} [f_i(\mathbf{r}, t) - f_i^{eq}(\mathbf{r}, t)] \quad (3)$$

$$f_i^{eq}(\mathbf{r}, t) = \rho w_i \left[1 + \frac{\mathbf{e}_i \cdot \mathbf{u}}{c_s^2} + \frac{(\mathbf{e}_i \cdot \mathbf{u})^2}{2c_s^4} - \frac{\mathbf{u}^2}{2c_s^2} \right] \quad (4)$$

where \mathbf{r} is the lattice node position and can be expressed in the Cartesian coordinate system as (x, y) , Δt is the time step, i is the direction index from 0 to 8, $f_i^{eq}(\mathbf{r}, t)$ is the Boltzmann equilibrium distribution, τ_f is the relaxation time for the Navier-Stokes flow, and c_s is the sound speed of the fluid and equals to $1/\sqrt{3}$ in dimensionless lattice unit. The weight factors are $w_0 = 4/9$, $w_{1-4} = 1/9$, and $w_{5-8} = 1/36$, respectively, in the D2Q9 model. The fluid density and velocity at each lattice node can be calculated by summing up the particle distribution functions in all the directions

$$\rho = \sum_i f_i \quad (5)$$

$$\rho \mathbf{u} = \sum_i f_i \mathbf{e}_i \quad (6)$$

The kinematic viscosity of fluid ν is related to the lattice relaxation time as

$$\nu = c_s^2 (\tau_f - 0.5) \Delta t \quad (7)$$

and the fluid pressure p is related to density as

$$p = \rho c_s^2 \quad (8)$$

2.2. Mass transfer

The mass transfer processes of CO₂ (denoted as 1) and CH₄ (denoted as 2) are simulated by two individual advection-diffusion equations

$$\partial_t C_1 + \nabla \cdot (C_1 \mathbf{u}) = \nabla \cdot (D_1 \nabla C_1) + R_1 \quad (9)$$

$$\partial_t C_2 + \nabla \cdot (C_2 \mathbf{u}) = \nabla \cdot (D_2 \nabla C_2) + R_2 \quad (10)$$

where C is the gas concentration, D is the bulk diffusion coefficient in the free space (i.e., bulk pore space), and R is the source/sink term implemented at the gas-solid boundary lattice nodes to mimic the surface adsorption/desorption and is set to zero in the free space. Assuming the typical Langmuir adsorption kinetics, the CO₂ adsorption R_1 can be expressed as an adsorption-desorption equilibrium [47]

$$R_1 = \frac{\partial N_1}{\partial t} = k_{a1} C_1 (N_{m1} - N_1) - k_{d1} N_1 \quad (11)$$

where N_m is the maximum gas adsorption amount, N is the current adsorption amount, and k_a (concentration⁻¹s⁻¹) and k_d (s⁻¹) are the adsorption and desorption rate constants, respectively. In the case of CO₂-CH₄ displacement, the solid matrix is initially saturated with CH₄ at the maximum N_{m2} . In the presence of CO₂, competitive adsorption takes place and the saturated CH₄ adsorption amount will be largely decreased to N_{m2}' due to the limited available adsorption sites and preferential adsorption of CO₂ [48]. The competitive adsorption process is simulated as fast CH₄ desorption that will decrease the CH₄ adsorption amount N_2 from N_{m2} to N_{m2}' when CO₂ reaches the lattice node, followed by a subsequent adsorption-desorption equilibrium

$$\begin{cases} R_2 = \frac{\partial N_2}{\partial t} = -k_{d2} N_2 & \text{if } N_2 > N_{m2}' \\ R_2 = \frac{\partial N_2}{\partial t} = k_{a2} C_2 (N_{m2}' - N_2) - k_{d2} N_2 & \text{if } N_2 \leq N_{m2}' \end{cases} \quad (12)$$

The threshold CO₂ concentration to trigger the competitive adsorption (i.e., when N_{m2} starts decreasing to N_{m2}') is set at 0.1 (lattice unit) in the simulations. The use of a small finite value of concentration instead of zero is to avoid the artificial non-zero concentration during numerical calculation. The Langmuir adsorption kinetics acts as the mass exchange between the free space and the solid matrix at the gas-solid boundary. Subsequently, the adsorbed gas evolves in a fully diffusive manner (i.e., advection velocity is zero) and propagates from the gas-solid boundary into the solid matrix interior under a concentration gradient for CO₂ and oppositely for CH₄ during desorption. The intra-matrix transport of adsorbed gas is described by the homogeneous solid diffusion model (HDSM) as [49]

$$\frac{\partial N_1}{\partial t} = D_{s1} \left(\frac{\partial^2 N_1}{\partial x^2} + \frac{\partial^2 N_1}{\partial y^2} \right) \quad (13)$$

$$\frac{\partial N_2}{\partial t} = D_{s2} \left(\frac{\partial^2 N_2}{\partial x^2} + \frac{\partial^2 N_2}{\partial y^2} \right) \quad (14)$$

where D_s is the gas diffusion coefficient in the solid matrix. The D2Q5 (two-dimensional and five-velocity) lattice model is used to solve the gas

concentration in the following five directions

$$\begin{cases} \text{Central : } \mathbf{e}_0 = (0, 0) \\ \text{Orthogonal : } \mathbf{e}_1 = (1, 0); \mathbf{e}_2 = (0, 1); \mathbf{e}_3 = (-1, 0); \mathbf{e}_4 = (0, -1) \end{cases}$$

The particle evolution function g_i at a time step is calculated as

$$g_i(\mathbf{r} + \Delta t \mathbf{e}_i, t + \Delta t) - g_i(\mathbf{r}, t) = -\frac{1}{\tau_c} [g_i(\mathbf{r}, t) - g_i^{eq}(\mathbf{r}, t)] \quad (15)$$

$$g_i^{eq}(\mathbf{r}, t) = C w_i \left(1 + \frac{\mathbf{e}_i \cdot \mathbf{u}}{c_s^2} \right) \quad (16)$$

where i is the direction index from 0 to 4, $g_i^{eq}(\mathbf{r}, t)$ is the Boltzmann equilibrium distribution, and τ_c is the relaxation time for advection-diffusion. The viscous gas flow velocity $\mathbf{u}(t)$ is retrieved from the Navier-Stokes lattice solution at each time step. The weight factors are $w_0 = 1/3$ and $w_{1-4} = 1/6$, respectively. The gas diffusion coefficient is related to the relaxation time according to

$$D = c_s^2 (\tau_c - 0.5) \Delta t \quad (17)$$

The gas concentration at each lattice node is obtained by summing up the particle distribution functions

$$C = \sum_i g_i \quad (18)$$

In order to take the source/sink term into account at the gas-solid boundary for mass exchange, the particle evolution function and related equations are simply modified as [50]

$$g_i(\mathbf{r} + \Delta t \mathbf{e}_i, t + \Delta t) - g_i(\mathbf{r}, t) = -\frac{1}{\tau_c} [g_i(\mathbf{r}, t) - g_i^{eq}(\mathbf{r}, t)] + q_i \Delta t \quad (19)$$

$$q_i = \left(1 - \frac{1}{2\tau_c} \right) w_i R \quad (20)$$

$$C = \sum_i g_i + \frac{1}{2} R \Delta t \quad (21)$$

where q_i is the discrete source/sink term for gas adsorption/desorption. It should be noted that each gas component has a set of solution lattices as described above. For the HDSM gas adsorption evolution inside the solid matrix, it is simply required to replace the concentration C by the gas adsorption amount N and τ_c by the relaxation time of D_s in Eqs. (15)–(18) with \mathbf{u} set to zero. The surface adsorption amount at the gas-solid boundary is recalculated at each time step according to Eqs. (11) and (12), and further acts as the boundary condition for gas adsorption evolution inside the solid matrix. The updated surface adsorption amount at the boundary after propagation into the solid matrix also has a feedback on the Langmuir adsorption kinetics by changing the adsorption and desorption rates. Therefore, surface adsorption/desorption only ceases when the entire solid matrix is saturated/desaturated with gas.

The above equations are implemented into OpenLB [51], an open-source numerical framework for LBM simulations. OpenLB provides a variety of 2D and 3D models with multiphysics coupling and can be easily executed on a parallel machine with distributed memory. Data visualization is conducted in ParaView [52]. The proposed LBM coupling scheme is concluded in four steps.

- The Navier-Stokes equations are solved in the bulk free space and each lattice node generates a velocity vector \mathbf{u} for the CO₂ and CH₄ mixture.
- In the free space, the advection-diffusion equations are solved for CO₂ and CH₄ on two separate lattices using the carrier fluid velocity \mathbf{u} determined from the Navier-Stokes lattice.

- c. At the gas-solid boundary, the dynamic surface gas adsorption amount is calculated through the source/sink term by the Langmuir adsorption kinetics.
- d. The adsorbed CO₂ diffuses from the gas-solid boundary into the solid matrix interior while CH₄ diffuses in the opposite direction during the desorption process.

To validate the LB model developed herein, we present three typical benchmark cases [40,53] for the coupled NSE-ADE scheme along with the prescribed boundary conditions. The first example illustrates the mass transfer process of Poiseuille flow through a plate channel with a reactive boundary (Fig. S1). The second example examines the pure diffusion process driven by a concentration gradient at zero velocity inside the solid matrix (Fig. S2). The third example validates the proposed model in simulating the stable counter-diffusion of a binary mixture between two parallel porous plates (Fig. S3). In the fourth example, we compare simulation results with experimental data where a CO₂-CH₄ mixture flows through a 26 cm-long dispersive packed bed column of activated carbon (Fig. S4) [54]. The LB model successfully reproduces results from the analytical solutions and the experiment. The validations are detailed in the supplementary material.

2.3. Boundary conditions

Boundary conditions are essential aspects to consider in the LBM simulations. As described in Section 2.2, the simulation domain comprises one Navier-Stokes lattice that solves the velocity field and two advection-diffusion lattices that solve the CO₂ and CH₄ concentrations, respectively. Therefore, each lattice requires a set of boundary conditions. The boundary conditions used in the simulations are summarized in Table 1 with a schematic drawing in Fig. 1. Except for the Langmuir adsorption kinetics at the solid surfaces and the fully developed concentration boundary condition at the outlet, all the other boundary conditions are already implemented in the framework of OpenLB and can be readily used for this application.

3. Results and discussion

The heterogeneous porous medium is created from a 2D image based on a slice of the realistic Berea sandstone rock sample [55]. Similar to Zhang and Sun [42], the rock property parameters are adjusted to match the characteristics of the shale matrix. Fig. 2 illustrates the construction of the LB model with the coupled mass transfer process. Before being read into the LB model, the 2D image is pre-processed in MATLAB to dilate the pore space and resize it to a suitable resolution corresponding to the lattice resolution. The final porous structure has a porosity of 0.48. We have tested the lattice spacing at resolutions of 344 × 340, 516 × 510, 774 × 765, 1161 × 1148, and 1742 × 1722 and found out that the concentration curves started to converge at 774 × 765. This lattice spacing has been selected to achieve a balance between computational accuracy and speed, which also ensures the resolution near the fluid-solid interfaces. The final pixel size is set to 3.6 nm (i.e., Δx = Δy = 3.6 nm), which leads to pore sizes ranging from 20 to 180 nm as shown in Fig. 3, consistent with the pore size distribution of the shale matrix. The pore size distribution is analyzed from the 2D image using the watershed segmentation algorithm developed by Rabbani et al. [56].

Table 1
Boundary conditions for the coupled NSE-ADE LB model.

Position	Navier-Stokes lattice	CO ₂ advection-diffusion lattice	CH ₄ advection-diffusion lattice
Inlet (lower)	$u = u_0$ (parabolic velocity profile)	$C_1 = C_0$ (constant concentration)	$C_2 = 0$ (no concentration)
Outlet (upper)	$p = p_0$ (constant pressure, open outlet)	$C_1^y = C_1^{y-1}$ (fully developed concentration, open outlet)	$C_2^y = C_2^{y-1}$ (fully developed concentration, open outlet)
Left	Bounce-back (no slip)	Bounce-back (no flux)	Bounce-back (no flux)
Right	Bounce-back (no slip)	Bounce-back (no flux)	Bounce-back (no flux)
Solid surfaces	Bounce-back (no slip)	Langmuir adsorption	Langmuir adsorption

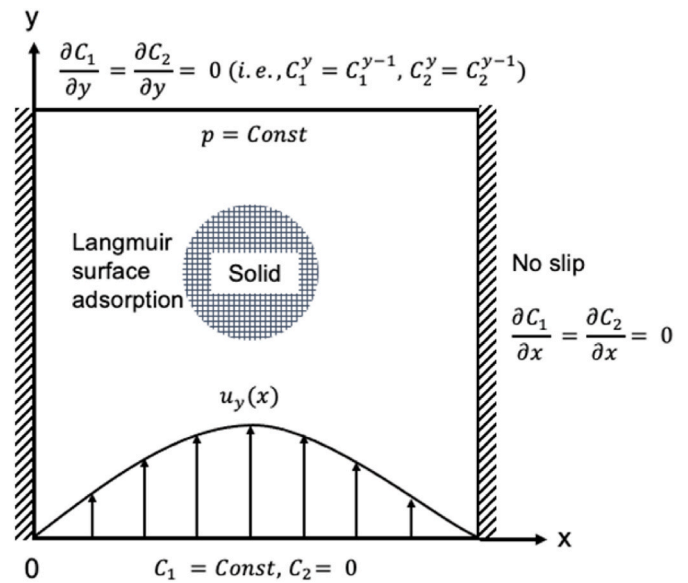


Fig. 1. A schematic drawing of the boundary conditions in the developed LB model.

The inlet and outlet are both extended with 50 additional rows of lattice nodes for the implementation of the boundary conditions and flow development. The number of additional rows of lattice nodes is examined to ensure the pressure drop across the simulation domain converges. The temperature in the simulation domain is set as 300 K. It is assumed that the residual CH₄ is at a depletion pressure of 1.8 MPa (0.75 kmol/m³) and the CO₂ injection pressure is 4.3 MPa (2.31 kmol/m³). Since both gas components have a similar viscosity under the relatively low-pressure conditions, the mixed gas interaction is neglected for simplicity, and the fictitious carrier fluid viscosity is assumed to be the average of the two. Although turbulent gas flow may occur in large natural and artificial fractures, shale matrix has extremely low permeability, and diffusion is usually considered the main gas transport mechanism in shale matrix. Herein, the simulations mainly focus on the laminar flow regime with a Reynolds number of 1.5. The local Reynolds number is estimated at 0.5–4.5 based on the pore velocity and pore size distribution. Low Reynolds numbers are characterized in similar numerical studies [27,41,57]. The maximum CO₂ and CH₄ adsorption amounts as well as the diffusion coefficients in the free space and kerogen matrix are referred from the previous MD studies [48,58]. The relaxation time parameters for viscosity, free diffusion, and solid diffusion are set as 1.29, 1.31, and 0.51, respectively, in the base case. They can be adjusted in the sensitivity study of diffusion coefficients according to Eqs. (7) and (17). The complete set of simulation parameters is described in Table 2, along with the conversion rules between the real and dimensionless lattice units. In this section, the effects of inter-matrix, interfacial, and intra-matrix mass transfer on the process of CO₂-CH₄ displacement are investigated in detail.

3.1. Effect of the solid diffusion coefficient

The mass transfer process consists of the intra-matrix and inter-

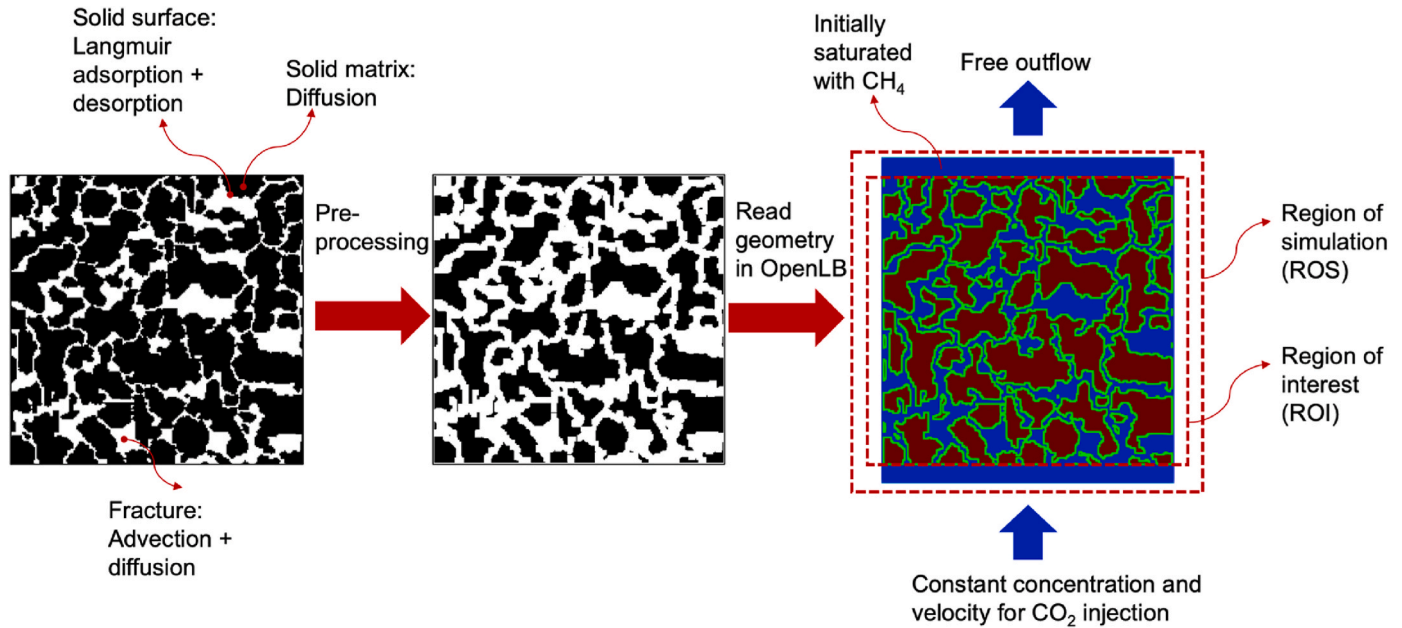


Fig. 2. Construction of the LB model in the simulation of CO₂-CH₄ displacement.

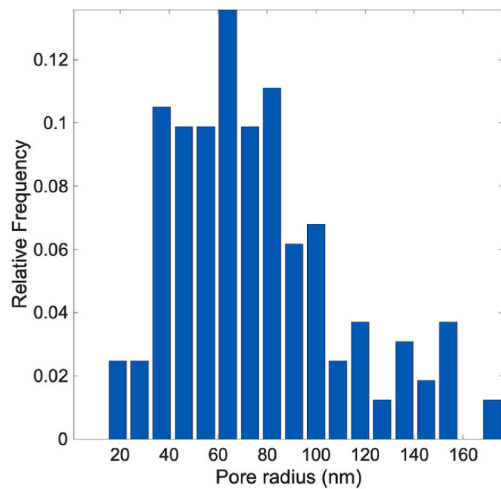


Fig. 3. Pore size distribution of the heterogeneous shale matrix geometry.

matrix components. Fig. 4 shows the concentration and adsorption evolutions of CO₂ and CH₄ at three stages in the nanoporous medium with the parameters described in Table 2 as the base case. It can be seen that the injected CO₂ advects in the free space, and surface adsorption happens quickly even at a low gas concentration. With the concentration increasing in the pore space, CO₂ starts to evolve into solids and saturates them toward the outlet. As for CH₄, the desorption in the solids is initiated by CO₂, the desorbed CH₄ transfers into the bulk phase and flows toward the outlet under the injection induced pressure gradient. The decreased concentration in the pore space further creates a concentration gradient between the bulk and the solid, leading to more CH₄ desorption from the solid matrix.

The results in Fig. 5 are normalized by the saturated gas concentration (C₁, C₂) and maximum adsorption amounts (N_{m1}, N_{m2}). They also show the recovery ratios of free (R_f) and adsorbed (R_s) CH₄ as the total gas amount is calculated from the multiplication of average concentration/adsorption and free space/solid lattice node number. The latter is cancelled out when calculating the ratio, which then becomes the same as our normalization. The total recovery ratio of CH₄ (free and adsorbed

Table 2

Simulation parameters and scaling relationships between physical and lattice units.

Parameter	Symbol	Physical value	Lattice value	Scaling ^a
ROI size	L _x	2.75 × 10 ⁻⁶ m	774	L _x = ΔxL̂ _x
	L _y	2.72 × 10 ⁻⁶ m	765	L _y = ΔyL̂ _y
Grid size	Δx	3.56 × 10 ⁻⁹ m	1	-
	Δy	3.56 × 10 ⁻⁹ m	1	-
Timestep	Δt	6.03 × 10 ⁻¹² s	1	-
Viscosity ^b	μ	5.54 × 10 ⁻⁷ m ² /s	0.264	μ = (Δx ² /Δt)μ̂
Injection velocity	v	0.2948 m/s	0.0005	v = (Δx/Δt)v̂
Saturated concentration ^b	C ₁	2.31 kmol/m ³	3.08	C ₁ = C ₂ Ĉ ₁
	C ₂	0.75 kmol/m ³	1	-
Diffusion coefficient in free space ^c	D ₁	5.66 × 10 ⁻⁷ m ² /s	0.27	D = (Δx ² /Δt)D̂
	D ₂	5.66 × 10 ⁻⁷ m ² /s	0.27	-
Diffusion coefficient in solid ^c	D _{s1}	6.71 × 10 ⁻⁹ m ² /s	0.0032	-
	D _{s2}	6.71 × 10 ⁻⁹ m ² /s	0.0032	-
Adsorption rate constant ^d	k _{a1}	2.21 × 10 ⁹ m ³ /kmol/s	0.01	k _a = (C ₂ ⁻¹ /Δt)k̂ _a
	k _{a2}	2.21 × 10 ⁹ m ³ /kmol/s	0.01	-
Desorption rate constant	k _{d1}	1.66 × 10 ⁷ s ⁻¹	0.0001	k _d = Δt ⁻¹ k̂ _c
	k _{d2}	1.66 × 10 ⁷ s ⁻¹	0.0001	-
Maximum adsorption ^e	N _{m1}	6 kmol/m ³	8	N _m = C ₂ N̂ _m
	N _{m2}	3.08 kmol/m ³	4.1	-
	N _{m2} '	0.45 kmol/m ³	0.6	-

^a Symbols for lattice values are expressed with a circumflex ^.

^b Referenced from the US National Institute of Standards and Technology (NIST) fluid properties data [59].

^c Referenced from Tesson and Firoozabadi [58]. The same base value is chosen for CO₂ and CH₄ to highlight the effect of other parameters, and different diffusion rates are studied as a selectivity in Section 3.2.

^d Referenced from Wang et al. [44].

^e Referenced from Wu et al. [48].

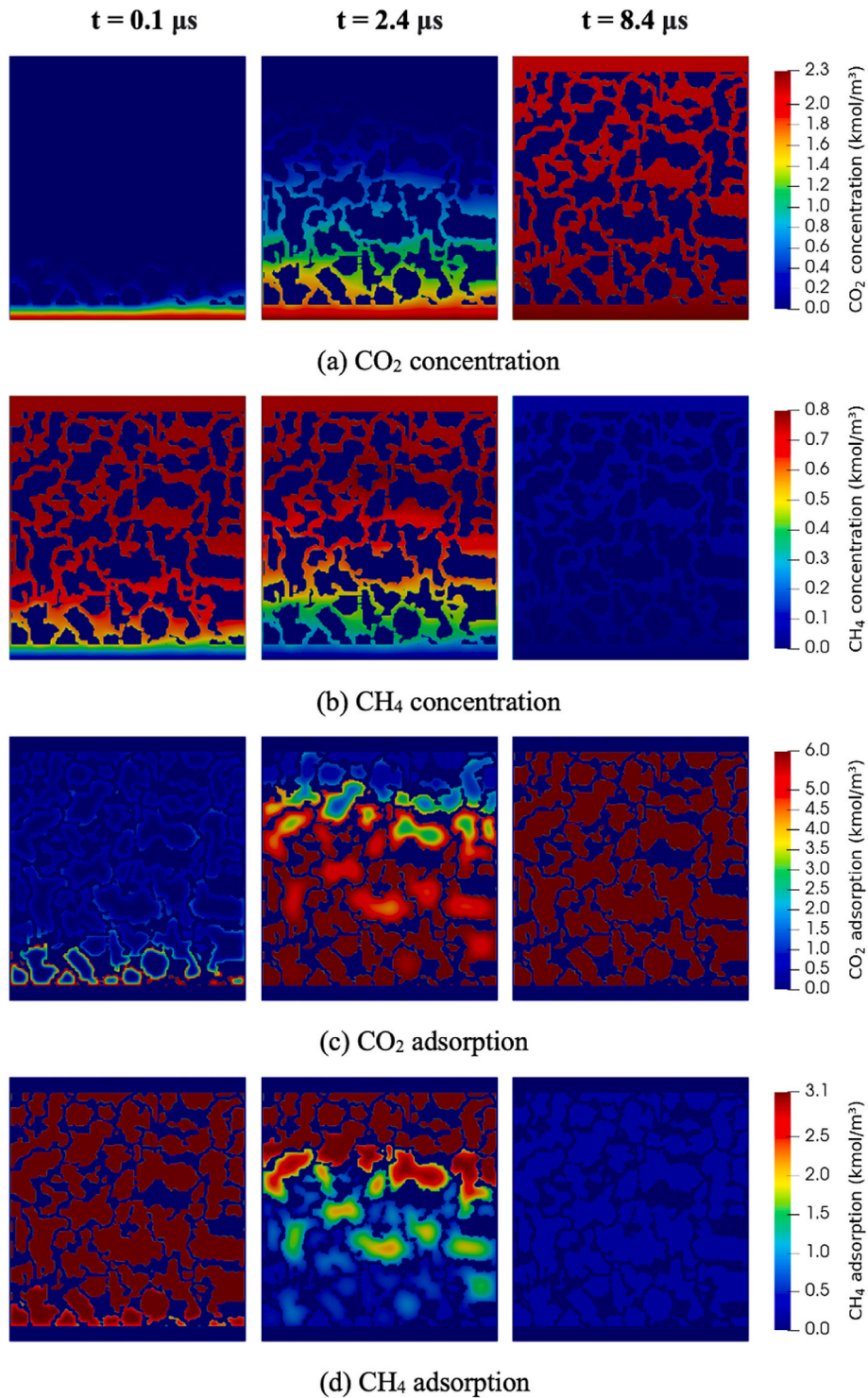


Fig. 4. CO₂ and CH₄ concentration (a–b) and adsorption (c–d) evolutions during the displacement at t = 0.1 μs, t = 2.4 μs, and t = 8.4 μs.

gases together) R_t can be easily converted from the normalized results as

$$R_t = \frac{R_f C_2 n + R_s N_{m2} (1 - n)}{C_2 n + N_{m2} (1 - n)} = \frac{0.36 R_f + 1.6016 R_s}{1.9616} \approx 0.18 R_f + 0.82 R_s \quad (22)$$

where, n is the porosity. Based on the figure, increasing the solid diffusion coefficient does not necessarily change the gas concentration and adsorption evolutions with time for both CO₂ and CH₄ (e.g., from D_s to $10D_s$). It can be attributed to the fact that gas diffusion rates in the solids have already reached a maximum point corresponding to the

adsorption and desorption reaction rates at the solid surfaces. In other words, the diffusion of adsorbed gas from the surfaces to solid interiors is limited by the surface adsorption kinetics. As the solid diffusion coefficient decreases, the intra-matrix mass transfer becomes weaker, as shown by the slower gas adsorption and desorption curves, which results in faster CO₂ saturation and CH₄ desaturation in the bulk free space. The rapid CH₄ desorption keeps the CH₄ bulk concentration stable for a longer period since the refilling from the adsorbed gas in the solids is immediate. In addition, the CH₄ desorption results in a significant gas concentration peak (>1) at the outlet, whose height increases with the

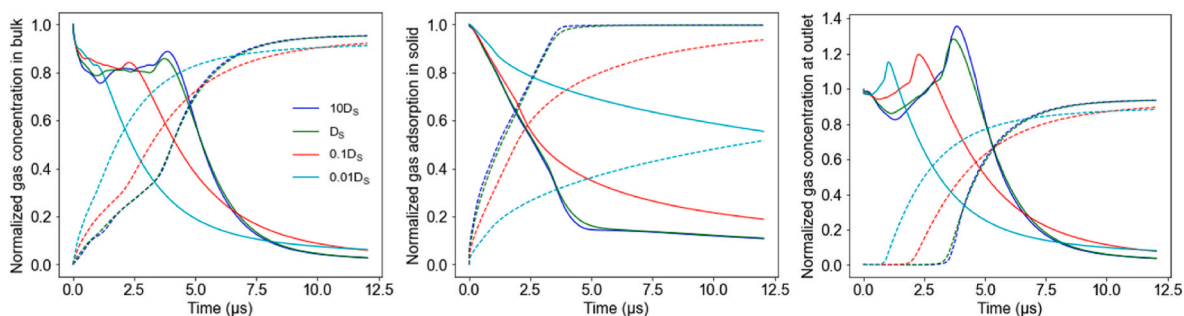


Fig. 5. Effects of gas diffusion coefficient (D_s) for both CO_2 and CH_4 in the solid matrix on CO_2 (dotted lines) and CH_4 (solid lines) concentration, adsorption, and outlet.

increasing desorption rate.

3.2. Transport selectivity in solid matrix

Transport selectivity is widely reported in MD studies where CO_2 and CH_4 show different mass transfer rates in nanopores. Our previous study suggests that the CO_2/CH_4 transport selectivity is within the range of 1–6 depending on the nanopore size and the total mixed gas pressure [60]. To investigate this effect at a large scale, we simulate the transport selectivity of CO_2/CH_4 by varying the diffusion coefficient of CO_2 in the solid matrix while keeping that of CH_4 the same. As shown in Fig. 6a, the CO_2/CH_4 selectivity nearly has no impact on the time-evolving gas concentration in the bulk and the gas adsorption in the solids when the solid diffusion coefficient is in the order of $10^{-9} \text{ m}^2/\text{s}$, which is two orders of magnitude smaller than that in the bulk free space. However, CO_2/CH_4 selectivity leads to significant differences in the bulk gas concentration and solid adsorption when the solid diffusion coefficient is decreased by two orders of magnitude (i.e., in the order of $10^{-11} \text{ m}^2/\text{s}$) as in Fig. 6b. It can also be seen that the CO_2/CH_4 selectivity mainly affects the CO_2 adsorption process in the solids while slightly affecting

the desorption of CH_4 . High CO_2 solid diffusion rates naturally result in a faster gas adsorption process. As the CO_2 adsorption rate increases in the solids, the bulk CO_2 is consumed faster and therefore takes a longer time to achieve saturation and reach the outlet. The CH_4 desaturation process is slightly faster in the bulk free space in the beginning at higher selectivities. This is possibly because the fast desorption of CH_4 (i.e., competitive adsorption) is triggered by CO_2 adsorption at the solid boundary, and therefore the evolution of CO_2 concentration can also affect CH_4 . The general results here indicate that the adsorption kinetics dominates the gas adsorption process under a fast gas diffusion rate in the solid matrix and selectivity is only non-negligible if the gas diffusion rate in solid is greatly lower than that in the bulk. It is suggested that gas separation can more easily achieve in porous media composed of low-permeable solid matrix.

3.3. Effect of surface adsorption/desorption rates

To study the effect of surface adsorption on the process of $\text{CO}_2\text{-CH}_4$ displacement, we run simulations with five groups of K_a/K_d from 10^1 to

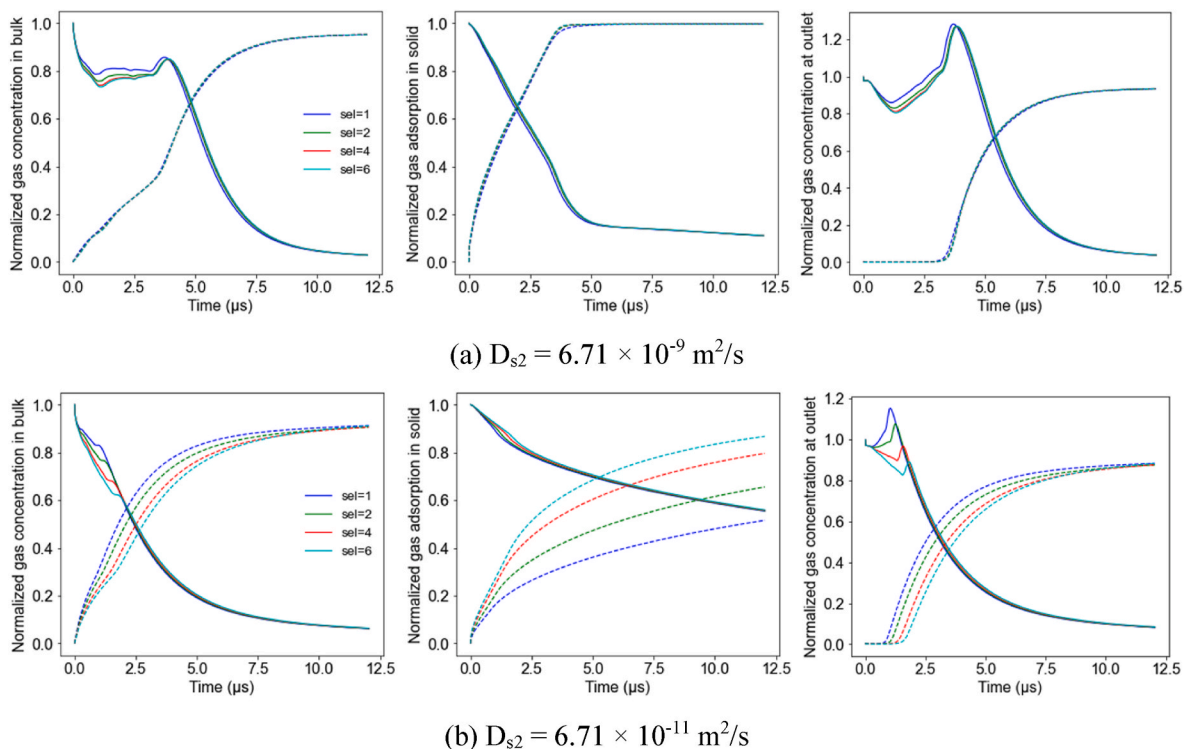


Fig. 6. Effects of CO_2/CH_4 transport selectivity (sel) in the solid matrix on CO_2 (dotted lines) and CH_4 (solid lines) concentration, adsorption, and outlet when (a) $D_{s2} = 6.71 \times 10^{-9} \text{ m}^2/\text{s}$ and (b) $D_{s2} = 6.71 \times 10^{-11} \text{ m}^2/\text{s}$, respectively.

10^3 . By fixing the desorption rate constant K_d , the relationships of both gas concentration in the bulk and gas adsorption in the solid matrix to varied adsorption rates K_a are obtained, as shown in Fig. 7a. It is noticeable that changing K_a alone does not generally affect either the CO_2 adsorption or the CH_4 desorption process in the bulk free space and solid matrix. This phenomenon suggests that the gas adsorption in the solids is limited by other mass transfer parameters such as solid diffusion coefficient and advection velocity. The Damkohler number ($Da = k_a L_x / D$) [61] compares the competition between reaction and diffusion, and it is estimated in the range of 3–287 based on 0.1– $10K_a$, which is much greater than one. Therefore, it may be a diffusion-limited state at the gas-solid interfaces under the studied conditions. When K_a is decreased to 0.1 of its base reference value, the CH_4 desorption speed increases, and the CO_2 maximum adsorption is not reached within the studied time frame.

Similarly, the desorption rate K_d has a negligible effect on the CO_2 adsorption process when K_a is fixed, according to Fig. 7b. In comparison, K_d can greatly affect the desorption process of CH_4 . As K_d increases, the CH_4 desorption from the solids becomes significantly faster since the CO_2 -initiated CH_4 desorption is directly proportional to K_d (i.e., $K_d C$). The fast-released CH_4 goes into the bulk free space and causes higher concentration peaks, as shown in the outflux concentrations.

3.4. Effect of pore geometry

The effect of pore geometry on the CO_2 – CH_4 displacement is investigated in four different particle-sized porous media S-1, S-2, S-3, and S-4 (Group 1) and in their duplicates with redistributed particle positions S-1*, S-2*, S-3*, and S-4* (Group 2), generated by the Quartet Structure Generation Set (QSGS) method [65] as presented in Fig. 8a. They are selected from a large dataset created by Germanou et al. [62], which intends to mimic the morphological features of the shale matrix. While the artificial pore geometries may still differ from the realistic case, the QSGS offers us the flexibility to study pore geometrical parameters (e.g., porosity, particle size, and particle aspect ratio) in a controlled way

while keeping the high heterogeneity similar to shale matrix. The porosity is kept at ~ 0.7 with varying particle numbers and sizes. The blockage ratio along the flow direction is shown in Fig. 8b, where its fluctuation decreases with the decreasing particle size. It is important to note that simplified 2D representations may overlook complex interconnections between pores, leading to an underestimation of the blockage ratio. The original image resolution is slightly changed to fit with the LB model resolution, as described in Table 2. Additionally, another group (Group 3) of simulations has been performed in S-1, S-2, S-3, and S-4 with the gas injection velocity reduced to 0.2v.

The same effect of pore geometry is identified in the three groups of simulations. It is found that the rearrangement of particle distribution nearly does not affect the adsorption-desorption process while the decreased gas injection velocity slightly delays the CO_2 – CH_4 displacement. As little difference is seen among the three groups of data, we only use the results from Group 1 as the representative case for the following detailed discussion on the effect of pore geometry. The results of time-evolving CO_2/CH_4 concentration, adsorption, and outflux at the outlet are included as Figs. S5 and S6 for Group 2 and Group 3, respectively, in the supplementary materials. According to Fig. 9, the particle size impacts both gas concentration in the bulk and gas adsorption in the solids. As the particle size decreases, the gas concentration and adsorption fronts travel slower and slower. The concentration front is also much flatter in small particle-sized porous structures such as S-3 and S-4. Fig. 10a provides a quantitative analysis of the pore geometry effect and confirms the faster evolution of gas concentration in porous media of large particle sizes. The transient adsorbed gas amount is higher for the large particle-sized porous structures, likely due to the decreased interparticle resistance to mass transfer. The ratio of the effective diffusion coefficient D_e to the bulk diffusion coefficient D is calculated for CO_2 according to [41,64]

$$D_e / D = \frac{\left(\int_0^{L_x} \left(\frac{\partial C}{\partial y} \right)_{y=L_y} dx \right) / L_x}{(C_{in} - C_{out}) / L_y} \quad (23)$$

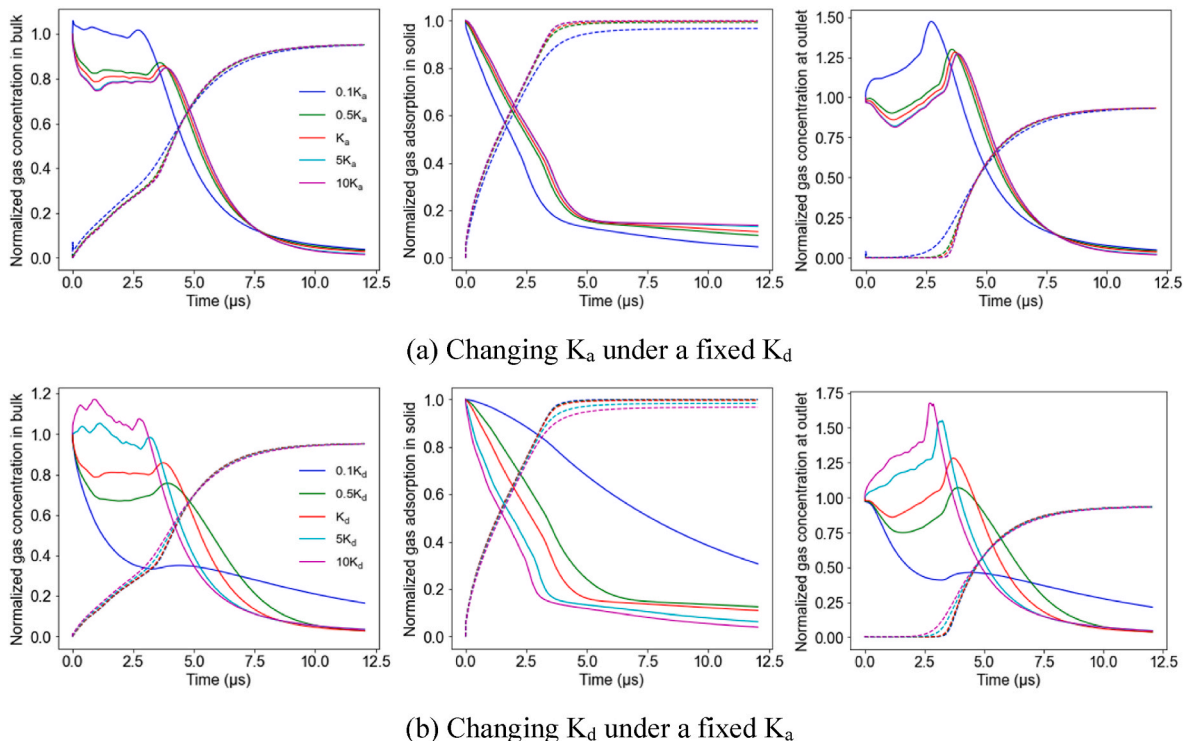


Fig. 7. Effects of adsorption (K_a) and desorption (K_d) rate constants on CO_2 (dotted lines) and CH_4 (solid lines) concentration, adsorption, and outflux when (a) K_d (b) K_a are fixed, respectively.

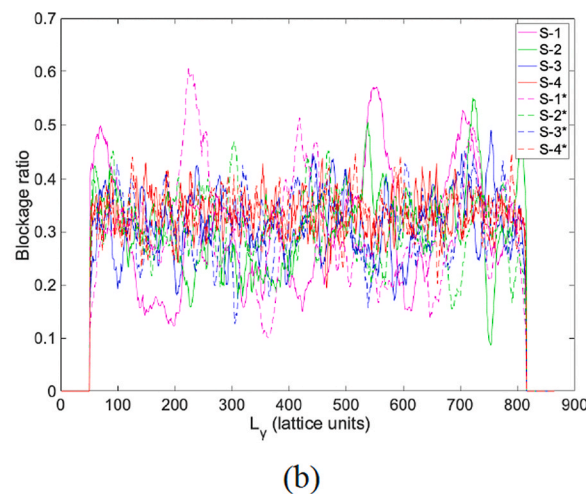
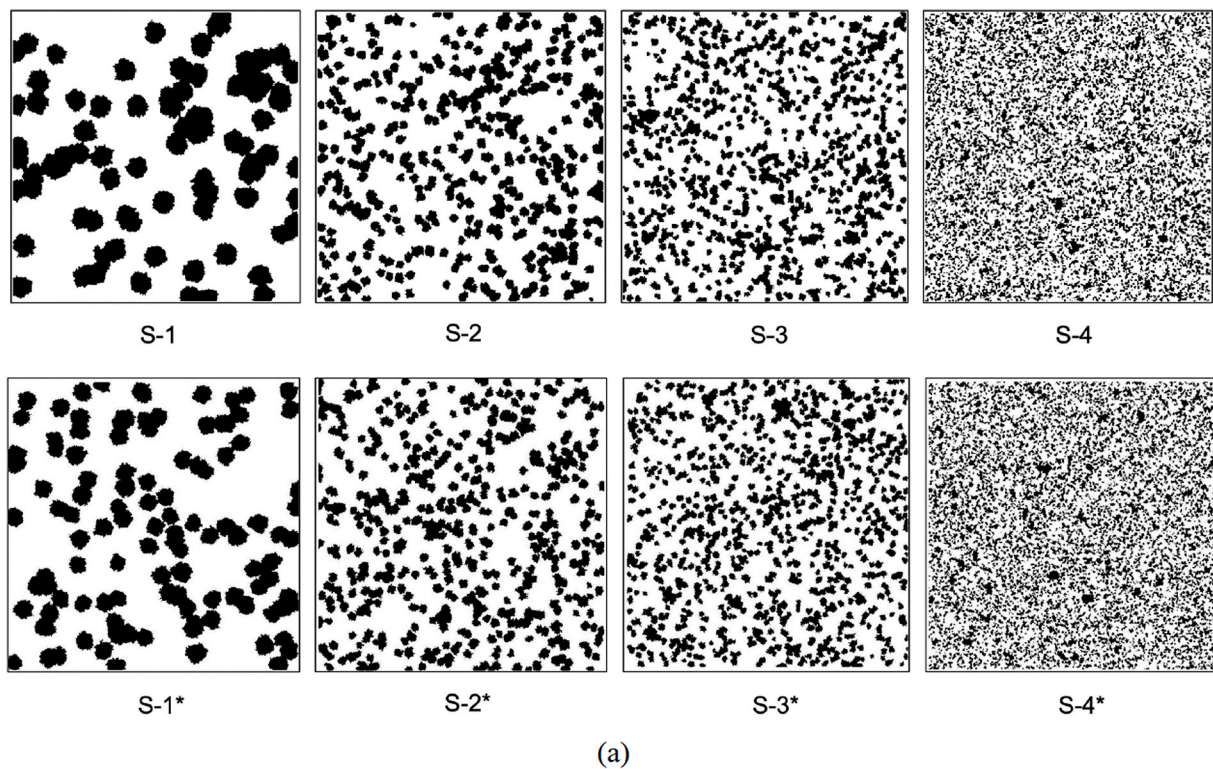


Fig. 8. (a) Random porous media generated by the Quartet Structure Generation Set (QSGS) method [62]. The average particle sizes d_p are 91.9 nm, 46.8 nm, 33.8 nm and 15.1 nm for S-1 to S-4 and 80.4 nm, 42.9 nm, 32.5 nm, and 15.4 nm for S-1* to S-4*, as analyzed by the method in Ref. [63]. (b) Blockage ratio of S-1 (*), S-2 (*), S-3 (*), and S-4 (*) along the flow direction L_y .

where C_{in} and C_{out} are the average inlet and outlet concentrations, respectively. A low ratio suggests more resistance during the mass transfer process in the porous medium. Additionally, permeability is calculated from Darcy's law

$$k = -\frac{\bar{v}\mu}{\nabla p} \quad (24)$$

where \bar{v} is the average bulk velocity. When CO_2 is being injected, it first saturates the interparticle free pore space through advection-diffusion. After CO_2 is brought to the solid surfaces, gas adsorption kinetics takes place, and the adsorbed CO_2 starts to diffuse toward the central region of the solids. With the decreasing particle size, the process of CO_2 adsorption becomes slower due to the decreased permeability that constrains advection in the free pore space, consistent with the observed

trend that both permeability and D_e/D decrease with the decreasing particle size in Fig. 10b. The results here are partially consistent with the findings of Zhou et al. [41], in which they suggest that intraparticle diffusion plays a dominant role in the mass transfer process of porous media with large solid particles, and interparticle advection-diffusion is instead more important in small particle-sized porous media. It is also mentioned that a fully developed flow field is achieved in the porous media of large particles and the gas concentration evolves more sufficiently in the pore spaces. However, they observe that the average adsorption uptake speed by the solids is in a nonmonotonic relationship with the particle size since increasing the particle size raises the intraparticle resistance at the same time. There exists an optimal point where the interparticle and intraparticle mass transfer rates are balanced with minimal total resistance. In comparison, CH_4 desorption is less sensitive to particle size change as the curves of S-1, S-2, and S-3 nearly collapse.

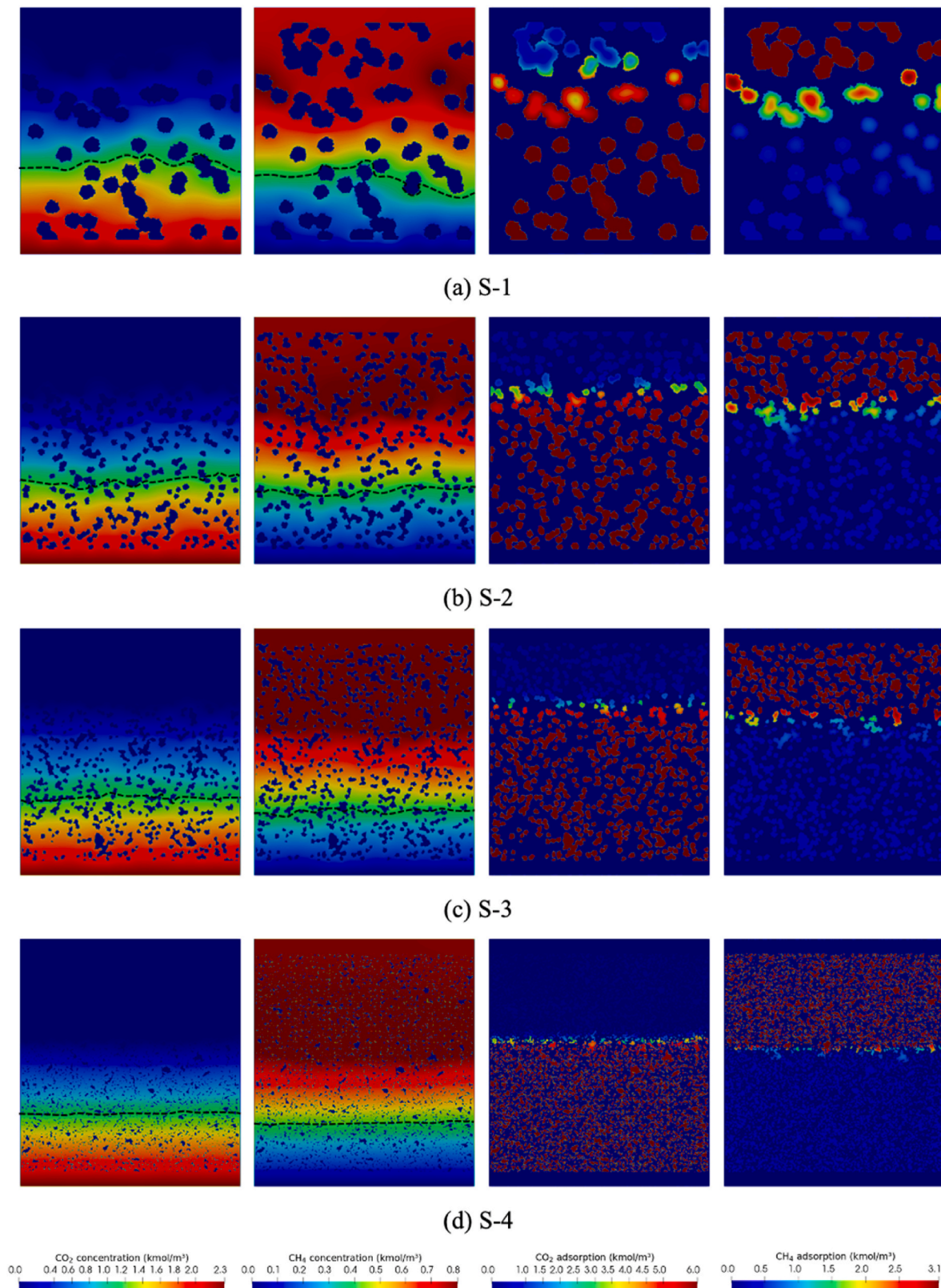


Fig. 9. Snapshots of CO₂ and CH₄ concentration and adsorption profiles in porous structures (a) S-1, (b) S-2, (c) S-3, and (d) S-4 at $t = 2.4 \mu\text{s}$. The black dotted lines show the 0.5-saturated concentration fronts.

The reason can be that desorption occurs in the opposite direction from the solid interior to the free space and thus may be less controlled by advection. Moreover, the CO₂ breakthrough curves at the outlet in Fig. 10c show that the CO₂-CH₄ displacement is faster in large

particle-sized porous media since CO₂ arrival and CH₄ depletion occur earlier at the outlet.

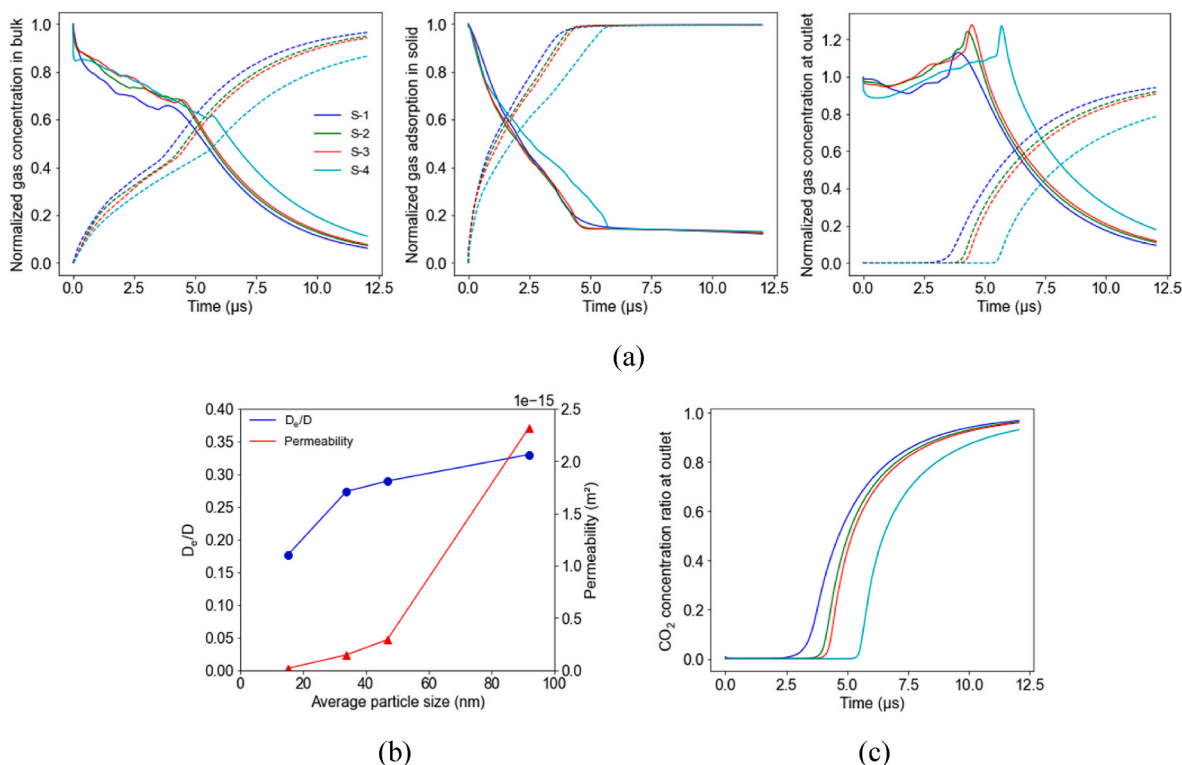


Fig. 10. (a) Effects of pore geometry on CO₂ (dotted lines) and CH₄ (solid lines) concentration, adsorption, and outflux. (b) The effective diffusion coefficient and permeability as a function of the average particle size. (c) CO₂ breakthrough curves at the outlet.

4. Conclusions

In this study, we have proposed an NSE-ADE coupling scheme in the LBM to study the CO₂–CH₄ displacement in the context of CO₂–ERG in the shale matrix. The global mass transfer process consists of advection-diffusion in the bulk free pore space, surface adsorption and desorption, and intra-matrix diffusion. Compared with MD, the proposed LB model is more time-efficient and can deal with complex pore geometries at microscale. Main conclusions are.

- Gas adsorption/desorption in the solid matrix is greatly impacted by the solid diffusion rate, which subsequently affects gas concentration in the bulk free space. Changing the adsorption rate constant between 2.21×10^8 and 2.21×10^{10} m³/kmol/s does not show a significant impact on gas adsorption or desorption while the desorption rate constant can largely control CH₄ desorption.
- The effect of CO₂/CH₄ selectivity is only pronounced in the less permeable solid matrix ($D_s = \sim 10^{-11}$ m²/s).
- Decreasing the particle size under a given porosity can constrain advection between solids in the pore space, leading to a slower adsorption/desorption process in the solid matrix. This slow-down further causes a delayed breakthrough curve for CO₂ at the outlet.

The results suggest that the CO₂–CH₄ displacement is likely more efficient in shale composed of a few large pieces of organic matrix instead of a great number of small ones under a given porosity. Increasing the matrix diffusion and desorption rates through fracturing can directly lead to faster CH₄ production. When upscaling, care should be given to CO₂/CH₄ transport selectivity if the gas diffusion rates in bulk and solids largely vary. Apart from the rigorous validations, the key parameters are physics-based and obtained from the actual cases characterizing the effect of confinement in nanoporous media. Therefore, the results are relevant to the actual process of CO₂–CH₄ displacement. The LB model herein simulates the CO₂–CH₄ displacement by separate ADEs

and the gas concentration change is assumed to not affect the viscous flow. It is recommended that the CO₂–CH₄ interaction, effect of adsorption on viscous flow, and nano-confinement should be included in future studies for more sophisticated investigation.

Credit author statement

Jian Wu: Conceptualization, Methodology, Investigation, Validation, Visualization, Writing – original draft. Yixiang Gan: Conceptualization, Writing – review & editing, Supervision. Zhang Shi: Methodology, Writing – review & editing. Pengyu Huang: Investigation, Writing – review & editing. Luming Shen: Conceptualization, Writing – review & editing, Supervision, Funding acquisition.

Declaration of competing interest

The authors declare that they have no known competing financial interests or personal relationships that could have appeared to influence the work reported in this paper.

Data availability

Data will be made available on request.

5. Acknowledgments

This work was supported in part by the Australian Research Council through Discovery Projects (DP200101919 and DP190102954). The authors acknowledge the use of the National Computational Infrastructure (NCI) which is supported by the Australian Government, and accessed through the Sydney Informatics Hub HPC Allocation Scheme, which is supported by the Deputy Vice-Chancellor (Research), University of Sydney.

Appendix A. Supplementary data

Supplementary data to this article can be found online at <https://doi.org/10.1016/j.energy.2023.127991>.

References

- [1] Alfarge D, Wei M, Bai B. Introduction to shale and tight oil reservoirs. *Developments in Petroleum Science*. Elsevier; 2020.
- [2] Klewiah I, Berawala DS, Alexander Walker HC, Andersen PØ, Nadeau PH. Review of experimental sorption studies of CO₂ and CH₄ in shales. *J Nat Gas Sci Eng* 2020; 73:103045.
- [3] Louk K, Ripepi N, Luxbacher K, Gilliland E, Tang X, Keles C, et al. Monitoring CO₂ storage and enhanced gas recovery in unconventional shale reservoirs: results from the Morgan County, Tennessee injection test. *J Nat Gas Sci Eng* 2017;45:11–25.
- [4] Fathi E, Akkutlu IY. Multi-component gas transport and adsorption effects during CO₂ injection and enhanced shale gas recovery. *Int J Coal Geol* 2014;123:52–61.
- [5] Xie W, Wang M, Chen S, Vandeginste V, Yu Z, Wang H. Effects of gas components, reservoir property and pore structure of shale gas reservoir on the competitive adsorption behavior of CO₂ and CH₄. *Energy* 2022;254:124242.
- [6] Yang X, Chen Z, Liu X, Xue Z, Yue F, Wen J, et al. Correction of gas adsorption capacity in quartz nanoslit and its application in recovering shale gas resources by CO₂ injection: a molecular simulation. *Energy* 2022;240:122789.
- [7] Iddphonce R, Wang J, Zhao L. Review of CO₂ injection techniques for enhanced shale gas recovery: prospect and challenges. *J Nat Gas Sci Eng* 2020;77:103240.
- [8] Huo P, Zhang D, Yang Z, Li W, Zhang J, Jia S. CO₂ geological sequestration: displacement behavior of shale gas methane by carbon dioxide injection. *Int J Greenh Gas Control* 2017;66:48–59.
- [9] Qin C, Jiang Y, Zuo S, Chen S, Xiao S, Liu Z. Investigation of adsorption kinetics of CH₄ and CO₂ on shale exposure to supercritical CO₂. *Energy* 2021;236:121410.
- [10] Zhang H, Moh DY, Wang X, Qiao R. Review on pore-scale physics of shale gas recovery dynamics: insights from molecular dynamics simulations. *Energy Fuel* 2022;36:14657–72.
- [11] Chen L, Huang D-B, Wang S-Y, Nie Y-N, He Y-L, Tao W-Q. A study on dynamic desorption process of methane in slits. *Energy* 2019;175:1174–80.
- [12] Yu H, Fan J, Chen J, Zhu Y, Wu H. Pressure-dependent transport characteristic of methane gas in slit nanopores. *Int J Heat Mass Tran* 2018;123:657–67.
- [13] Nan Y, Li W, Jin Z. Slip length of methane flow under shale reservoir conditions: effect of pore size and pressure. *Fuel* 2020;259:116237.
- [14] Wang S, Feng Q, Javadpour F, Zha M, Cui R. Multiscale modeling of shale apparent permeability: an integrated study of molecular dynamics and pore network model. *SPE Annual Technical Conference and Exhibition*. OnePetro; 2017.
- [15] Zhan S, Su Y, Lu M, Cai M, Fu J, Liu Z, et al. Effect of surface type on the flow characteristics in shale nanopores. *Geofluids* 2021;2021:1–12.
- [16] Yu H, Fan J, Xia J, Liu H, Wu H. Multiscale gas transport behavior in heterogeneous shale matrix consisting of organic and inorganic nanopores. *J Nat Gas Sci Eng* 2020;75:103139.
- [17] Castez MF, Winograd EA, Sánchez VM. Methane flow through organic-rich nanopores: the key role of atomic-scale roughness. *J Phys Chem C* 2017;121(51): 28527–36.
- [18] Yu H, Xu H, Fan J, Wang F, Wu H. Roughness factor-dependent transport characteristic of shale gas through amorphous kerogen nanopores. *J Phys Chem C* 2020;124(23):12752–65.
- [19] Zhao Y, Luo M, Liu L, Wu J, Chen M, Zhang L. Molecular dynamics simulations of shale gas transport in rough nanopores. *J Petrol Sci Eng* 2022;217:110884.
- [20] He J, Ju Y, Kulasinski K, Zheng L, Lammers L. Molecular dynamics simulation of methane transport in confined organic nanopores with high relative roughness. *J Nat Gas Sci Eng* 2019;62:202–13.
- [21] Huang P, Shen L, Maggi F, Chen Z, Pan Z. Influence of surface roughness on methane flow in shale kerogen nano-slits. *J Nat Gas Sci Eng* 2022:104650.
- [22] Fang T, Wang M, Gao Y, Zhang Y, Yan Y, Zhang J. Enhanced oil recovery with CO₂/N₂ slug in low permeability reservoir: molecular dynamics simulation. *Chem Eng Sci* 2019;197:204–11.
- [23] Zhang W, Feng Q, Wang S, Xing X, Jin Z. CO₂-regulated octane flow in calcite nanopores from molecular perspectives. *Fuel* 2021;286:119299.
- [24] Collell J, Galliero G, Vermorel R, Ungerer P, Yiannourakou M, Montel F, et al. Transport of multicomponent hydrocarbon mixtures in shale organic matter by molecular simulations. *J Phys Chem C* 2015;119(39):22587–95.
- [25] Krüger T, Kusumaatmaja H, Kuzmin A, Shardt O, Silva G, Viggien EM. The lattice Boltzmann method. Springer International Publishing 2017;10(978–3):4–15.
- [26] Wang H, Chen L, Qu Z, Yin Y, Kang Q, Yu B, et al. Modeling of multi-scale transport phenomena in shale gas production — a critical review. *Appl Energy* 2020;262: 114575.
- [27] Yan M, Zhou M, Li S, Lin H, Zhang K, Zhang B, et al. Numerical investigation on the influence of micropore structure characteristics on gas seepage in coal with lattice Boltzmann method. *Energy* 2021;230:120773.
- [28] Sheikholeslami M, Gorji-Bandpy M, Ganji D. Numerical investigation of MHD effects on Al₂O₃–water nanofluid flow and heat transfer in a semi-annulus enclosure using LBM. *Energy* 2013;60:501–10.
- [29] Zhou W, Yang X, Liu X. Multiscale modeling of gas flow behaviors in nanoporous shale matrix considering multiple transport mechanisms. *Phys Rev E* 2022;105 (5–2):055308.
- [30] Wang J, Chen L, Kang Q, Rahman SS. The lattice Boltzmann method for isothermal micro-gaseous flow and its application in shale gas flow: a review. *Int J Heat Mass Tran* 2016;95:94–108.
- [31] Liu L, Wang Y, Aryana SA. Insights into scale translation of methane transport in nanopores. *J Nat Gas Sci Eng* 2021;96:104220.
- [32] Wang J, Kang Q, Wang Y, Pawar R, Rahman SS. Simulation of gas flow in micro-porous media with the regularized lattice Boltzmann method. *Fuel* 2017;205: 232–46.
- [33] Wang J, Kang Q, Chen L, Rahman SS. Pore-scale lattice Boltzmann simulation of micro-gaseous flow considering surface diffusion effect. *Int J Coal Geol* 2017;169: 62–73.
- [34] Zhao J, Yao J, Zhang L, Sui H, Zhang M. Pore-scale simulation of shale gas production considering the adsorption effect. *Int J Heat Mass Tran* 2016;103: 1098–107.
- [35] Wang H, Su Y, Wang W, Jin Z, Chen H. CO₂-oil diffusion, adsorption and miscible flow in nanoporous media from pore-scale perspectives. *Chem Eng J* 2022;450: 137957.
- [36] Peng Z, Liu S, Tang S, Zhao Y, Li Y. Multicomponent lattice Boltzmann simulations of gas transport in a coal reservoir with dynamic adsorption. *Geofluids* 2018;2018: 1–13.
- [37] Lei J, Ding R, Zhang J. Study on seepage and adsorption characteristics of porous media containing adsorbent based on lattice Boltzmann. *AIP Adv* 2021;11(4): 045126.
- [38] Zakirov TR, Khramchenkov MG. Effect of pore space heterogeneity on the adsorption dynamics in porous media at various convection-diffusion and reaction conditions: a lattice Boltzmann study. *J Petrol Sci Eng* 2022;212:110300.
- [39] Peng Z, Deng Z, Feng H, Liu S, Li Y. Multiscale lattice Boltzmann simulation of the kinetics process of methane desorption-diffusion in coal. *ACS Omega* 2021;6(30): 19789–98.
- [40] Zhou L, Qu ZG, Chen L, Tao WQ. Lattice Boltzmann simulation of gas–solid adsorption processes at pore scale level. *J Comput Phys* 2015;300:800–13.
- [41] Zhou L, Qu ZG, Ding T, Miao JY. Lattice Boltzmann simulation of the gas–solid adsorption process in reconstructed random porous media. *Phys Rev E* 2016;93: 043101.
- [42] Zhang T, Sun S. A coupled Lattice Boltzmann approach to simulate gas flow and transport in shale reservoirs with dynamic sorption. *Fuel* 2019;246:196–203.
- [43] Jiang M, Xu ZG. Pore-scale investigation on reactive flow in non-uniform dissolved porous media considering immiscible phase by lattice Boltzmann method. *J Nat Gas Sci Eng* 2021;96:104280.
- [44] Wang H, Qu ZG, Zhou L. Coupled GCMC and LBM simulation method for visualizations of CO₂/CH₄ gas separation through Cu-BTC membranes. *J Membr Sci* 2018;550:448–61.
- [45] Xia M. Pore-scale simulation of miscible displacement in porous media using the lattice Boltzmann method. *Comput Geosci* 2016;88:30–40.
- [46] Bhatnagar PL, Gross EP, Krook M. A model for collision processes in gases. I. Small amplitude processes in charged and neutral one-component systems. *Phys Rev* 1954;94(3):511.
- [47] He X, Li N, Goldstein B. Lattice Boltzmann simulation of diffusion-convection systems with surface chemical reaction. *Mol Simulat* 2000;25(3–4):145–56.
- [48] Wu J, Huang P, Maggi F, Shen L. Molecular investigation on CO₂-CH₄ displacement and kerogen deformation in enhanced shale gas recovery. *Fuel* 2022;315:123208.
- [49] Chahbani M, Labidi J, Paris J. Effect of mass transfer kinetics on the performance of adsorptive heat pump systems. *Appl Therm Eng* 2002;22(1):23–40.
- [50] Seta T. Implicit temperature-correction-based immersed-boundary thermal lattice Boltzmann method for the simulation of natural convection. *Phys Rev* 2013;87(6): 063304.
- [51] Krause MJ, Kummerländer A, Avis SJ, Kusumaatmaja H, Dapelo D, Klemens F, et al. OpenLB—open source lattice Boltzmann code. *Comput Math Appl* 2021;81: 258–88.
- [52] Henderson A. Para view guide: a parallel visualization application. Clifton Park, NY: Kitware, Inc; 2007.
- [53] Inamuro T, Yoshino M, Inoue H, Mizuno R, Ogino F. A lattice Boltzmann method for a binary miscible fluid mixture and its application to a heat-transfer problem. *J Comput Phys* 2002;179(1):201–15.
- [54] Mansoubi H, Mansourpour Z, Fatemi S. Investigation of CO(2) and CH(4) capture from syngas in adsorption process and breakthrough modeling by modified Lattice-Boltzmann mesoscale method. *Chemosphere* 2023;325:138366.
- [55] Boek ES, Venturoli M. Lattice-Boltzmann studies of fluid flow in porous media with realistic rock geometries. *Comput Math Appl* 2010;59(7):2305–14.
- [56] Rabbani A, Jamshidi S, Salehi S. An automated simple algorithm for realistic pore network extraction from micro-tomography images. *J Petrol Sci Eng* 2014;123: 164–71.
- [57] Zhao T, Zhao H, Li X, Ning Z, Wang Q, Zhao W, et al. Pore scale characteristics of gas flow in shale matrix determined by the regularized lattice Boltzmann method. *Chem Eng Sci* 2018;187:245–55.
- [58] Tesson S, Firoozabadi A. Methane adsorption and self-diffusion in shale kerogen and slit nanopores by molecular simulations. *J Phys Chem C* 2018;122(41): 23528–42.
- [59] Linstrom P, Mallard W. NIST chemistry WebBook, NIST standard reference database number 69. Gaithersburg MD: National Institute of Standards and Technology; 2022, 20899.
- [60] Wu J, Shen L, Huang P, Gan Y. Selective adsorption and transport of CO₂-CH₄ mixture under nano-confinement. *Energy* 2023;273:127224.
- [61] Kang Q, Chen L, Valocchi AJ, Viswanathan HS. Pore-scale study of dissolution-induced changes in permeability and porosity of porous media. *J Hydrol* 2014;517: 1049–55.

- [62] Germanou L, Ho MT, Zhang Y, Wu L. Intrinsic and apparent gas permeability of heterogeneous and anisotropic ultra-tight porous media. *J Nat Gas Sci Eng* 2018; 60:271–83.
- [63] Rabbani A, Ayatollahi S. Comparing three image processing algorithms to estimate the grain-size distribution of porous rocks from binary 2D images and sensitivity analysis of the grain overlapping degree. *Spec Top Rev Porous Media Int J* 2015;6 (1).
- [64] Mu D, Liu Z-S, Huang C, Djilali N. Prediction of the effective diffusion coefficient in random porous media using the finite element method. *J Porous Mater* 2007;14(1): 49–54.
- [65] Wang M, Wang J, Pan N, Chen S. Mesoscopic predictions of the effective thermal conductivity for microscale random porous media. *Phys Rev E* 2007;75(3):036702.